Supplementary materials for

Active nematic liquid crystals simulated by particle-based mesoscopic methods

J. Macías-Durán, V. Duarte-Alaniz, and H. Híjar

Abstract

This document includes: Appendices A to F, Figures S 1 to S6, and Legends for movies S1 to S14. **Other supplementary files for this paper include**: Movies S1 to S14.

A Finite difference approximation to gradients

MPCD cells are centered at positions of a cubic lattice $x_{\alpha,i} = ia$, for $\alpha = 1,2,3$, $i = 1,2,\ldots,n_{\text{cells}}$, and $n_{\text{cells}} = V^{1/3}/a$, is the number of collision cells along any one of the Cartesian axes. Each cell is associated univocally to a vector $(x_{1,i}, x_{2,j}, x_{3,k})$. We approximated spatial derivatives by centered finite differences [1] as follows. The velocity gradient and the divergence of $Q^{\text{c}}_{\alpha\beta}$ were calculated, respectively, from

$$\nabla_\beta v^{\text{c}}_\alpha = \frac{v^{\text{c}}_\alpha\left(x_{\beta,i+1}\right) - v^{\text{c}}_\alpha\left(x_{\beta,i-1}\right)}{2a},$$

and

$$\nabla_\mu Q^{\text{c}}_{\mu\alpha} = \frac{Q^{\text{c}}_{1\alpha}\left(x_{1,i+1}\right) - Q^{\text{c}}_{1\alpha}\left(x_{1,i-1}\right)}{2a} + \frac{Q^{\text{c}}_{2\alpha}\left(x_{2,j+1}\right) - Q^{\text{c}}_{2\alpha}\left(x_{2,j-1}\right)}{2a} + \frac{Q^{\text{c}}_{3\alpha}\left(x_{3,k+1}\right) - Q^{\text{c}}_{3\alpha}\left(x_{3,k-1}\right)}{2a},$$

where the unwritten arguments of v^{c}_α and $Q^{\text{c}}_{\mu\alpha}$ remain constant at cell's center. We took into account periodic boundary conditions by applying $v^{\text{c}}_\alpha\left(x_{\beta,n_{\text{cells}}+1}\right) = v^{\text{c}}_\alpha\left(x_{\beta,1}\right)$, $v^{\text{c}}_\alpha\left(x_{\beta,0}\right) = v^{\text{c}}_\alpha\left(x_{\beta,n_{\text{cells}}}\right)$, $Q^{\text{c}}_{\alpha\beta}\left(x_{\mu,n_{\text{cells}}+1}\right) = Q^{\text{c}}_{\alpha\beta}\left(x_{\mu,1}\right)$, and $Q^{\text{c}}_{\alpha\beta}\left(x_{\mu,0}\right) = Q^{\text{c}}_{\alpha\beta}\left(x_{\mu,n_{\text{cells}}}\right)$, when necessary.

We also calculated second order derivatives under the central approximation scheme, e.g., for the Laplacian of $Q^{\text{c}}_{\alpha\beta}$ we used

$$\begin{aligned}\nabla^2_\mu Q^{\text{c}}_{\alpha\beta} &= \frac{Q^{\text{c}}_{\alpha\beta}\left(x_{1,i+1}\right) + Q^{\text{c}}_{\alpha\beta}\left(x_{1,i-1}\right) - 2Q^{\text{c}}_{\alpha\beta}\left(x_{1,i}\right)}{a^2} \\ &+ \frac{Q^{\text{c}}_{\alpha\beta}\left(x_{2,j+1}\right) + Q^{\text{c}}_{\alpha\beta}\left(x_{2,j-1}\right) - 2Q^{\text{c}}_{\alpha\beta}\left(x_{2,j}\right)}{a^2} \\ &+ \frac{Q^{\text{c}}_{\alpha\beta}\left(x_{3,k+1}\right) + Q^{\text{c}}_{\alpha\beta}\left(x_{3,k-1}\right) - 2Q^{\text{c}}_{\alpha\beta}\left(x_{3,k}\right)}{a^2}.\end{aligned}$$

B Physical parameters of OCO based AN-MPCD

In the one-constant approximation, elasticity is related with order correlation functions as [2–4]

$$\langle \hat{Q}_{\alpha 3}(\mathbf{k}) \hat{Q}^*_{\alpha 3}(\mathbf{k}) \rangle = \frac{1}{2} \frac{V k_{\text{B}} T}{L\left(k^2_\alpha + k^2_3\right)}, \tag{B1}$$

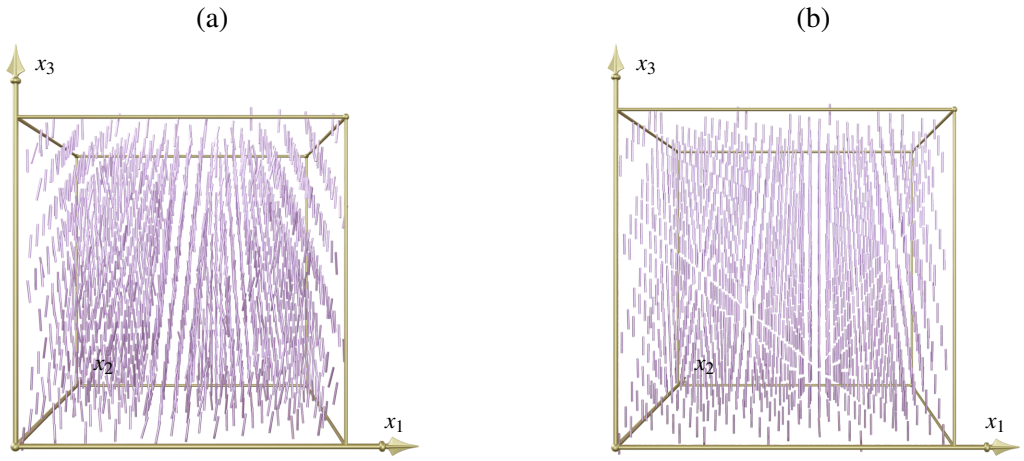

Figure S 1: Snapshots of the orientation states in simulated passive nematics ($\zeta = 0$). (a) OCO based AN-MPCD at $U = 25\,k_\mathrm{B}T$. (b) Hybrid based AN-MPCD.

and [5]

$$\langle \delta\tilde{n}_\alpha(\mathbf{k},\omega)\,\delta\tilde{n}^*_\alpha(\mathbf{k},\omega)\rangle = \frac{2(2\pi)^4\gamma_1 V\mathscr{T}k_\mathrm{B}T}{\omega^2+(K/\gamma_1)^2k^4}. \tag{B2}$$

In equations (B1) and (B2) circumflex and tilde accents indicate the space and time–space Fourier transform, respectively; $\gamma_1 = 2\mu_1/(9S^2)$; [6] ω is the frequency; $\mathscr{T}$ is the scattering time; $\langle\ldots\rangle$ is the time average; and * denotes complex conjugate. Also, no summation over repeated indices is implied and $\alpha = 1,2$.

For calculations we proceed similarly as in references [4, 5]. To estimate L, we fitted equation (B1) for four wave numbers ($k_1 = 2\pi j/V^{1/3}$, $j = 1,2,3,4$; and $k_2 = k_3 = 0$). K/γ_1 was obtained by fitting the half-width at half-height of director correlations using $k_1 = 2\pi/V^{1/3}$.

To calculate ξ_N, we assumed that f_ori in equation (4) can be used to generate a hierarchy of equations for multipolar order parameters, as in various kinetic models of liquid crystals. [7–9] When this hierarchy is cut at the quadrupolar order and closed by the Doi–Hess decoupling approximation, $\langle u^i_\alpha u^i_\beta u^i_\gamma u^i_\delta\rangle = \langle u^i_\alpha u^i_\beta\rangle\langle u^i_\gamma u^i_\delta\rangle$, [10] material ordering is described by a free energy of the LdG type. [11] This permits to identify $\alpha_\mathsf{F} = 6\mathscr{D}\mu_1\,[1-U/(3k_\mathrm{B}T)]$, $\beta_\mathsf{F} = -4\mathscr{D}\mu_1 U/(3k_\mathrm{B}T)$, and $\gamma_\mathsf{F} = 2\mathscr{D}\mu_1 U/(3k_\mathrm{B}T)$. Here, $\mathscr{D}$ is the rotational diffusion coefficient that was approximated in terms of the relaxation of director correlations, $\langle(n_\alpha(t)-n_\alpha(0))\,(n_\alpha(t)-n_\alpha(0))\rangle \simeq 4\mathscr{D}t$, where summation over repeated indices is reassumed. [12] We obtained, $\mathscr{D} \simeq 0.014$, 0.015, 0.023, and $0.039\,t_0^{-1}$ for $U = 15$, 20, 25, and $30\,k_\mathrm{B}T$, respectively. We used measurements of S, L and K/γ_1 to calculate the corresponding values of μ_1 and, subsequently, LdG coefficients. Finally, equation (13) yields ξ_N as reported in table 1.

C Passive nematic states

When $\zeta = 0$, OCO based and Hybrid based AN-MPCD yield stable nematic phases in which the director field points along the x_3 axis. Passive orientation configurations obtained after thermalization are illustrated in figure S 1 (a) and (b) for OCO based AN-MPCD at $U = 25\,k_\mathrm{B}T$ and Hybrid based AN-MPCD, respectively.

D Calculation of correlation functions and spectra

We obtained averages in equation (19) by using the ensemble of AN-MPCD particles and their velocities over different time-steps. Correlation at instant t was calculated from contributions of all particles located within spherical shells of radius R and width ΔR, centered at positions $r^i_\alpha(t)$. The average over all particles in the system yields

$$\langle \bar{v}_\alpha(\mathbf{R}+\mathbf{r}(t))\,\bar{v}_\alpha(\mathbf{r}(t))\rangle \simeq \frac{1}{2N}\sum_{i=1}^{N}\left\{\frac{1}{N_i(R)}\sum_{R_\mathrm{i}<r^{ij}(t)\leq R_\mathrm{o}}\bar{v}^j_\alpha(t)\,\bar{v}^i_\alpha(t)\right\}, \tag{D1}$$

where $r^{ij}(t)=|\mathbf{r}^j(t)-\mathbf{r}^i(t)|$; $R_\mathrm{i}=R-\Delta R/2$ and $R_\mathrm{o}=R+\Delta R/2$ are the internal and external radii of the shell, respectively; and

$$N_i(R)=\sum_{R_\mathrm{i}<r^{ij}(t)\leq R_\mathrm{o}} 1. \tag{D2}$$

Then, we obtained $C_\mathrm{v}(R)$ after time averaging $\langle \bar{v}_\alpha(\mathbf{R}+\mathbf{r}(t))\,\bar{v}_\alpha(\mathbf{r}(t))\rangle$ and normalising.

In the case of energy spectra in equations (21) and (22), we calculated first the instantaneous three-dimensional energy densities

$$E_\mathrm{kin}(\mathbf{k}';t)=\frac{1}{2(2\pi)^3}\frac{\rho}{V}\hat{v}_\alpha(\mathbf{k}';t)\,\hat{v}^*_\alpha(\mathbf{k}';t), \tag{D3}$$

and

$$E_\mathrm{ela}(\mathbf{k}';t)=\frac{1}{2(2\pi)^3}\frac{L}{V}k'^2\hat{Q}_{\alpha\beta}(\mathbf{k}';t)\,\hat{Q}^*_{\alpha\beta}(\mathbf{k}';t), \tag{D4}$$

from discrete Fourier transforms of flow and orientation at time t. Due to the finite size of the simulation boxes and the periodicity of boundary conditions, permitted values of the wave vector are discrete, namely, $k_\alpha = jk_\mathrm{min}$, where $k_\mathrm{min}=2\pi/(V)^{1/3}$ and $j=1,2,\ldots,n_\mathrm{cells}$.

$E_\mathrm{kin}(\mathbf{k}';t)$ and $E_\mathrm{ela}(\mathbf{k}';t)$ are averaged by summing contributions of the discrete points located within spherical shells of radius $k=jk_\mathrm{min}$ and width $\Delta k=k_\mathrm{min}$. Finally, results are averaged over time.

E Rescaled correlation functions

Correlations functions $C_\mathrm{v}(R)$ and $C_\mathrm{W}(R)$, as well as spectra $E_\mathrm{ela}(k)$ and $E_\mathrm{kin}(k)$, exhibit universal scaling behaviour which can be revealed by rescaling lengths and correlation values in figures 9-12. Curves for C_v and C_W collapse when they are plotted as function of the normalized radial distance R/l_v. This is illustrated in figure S 2.

In OCO based AN-MPCD, l_v and l_W fall on single curves when they are given in units of the collision cell size a. This is shown in figure S 3 which was obtained from data in figures 10 (a) and (c) multiplied by $\xi_\mathrm{N}(U)$ given in table 1.

Elastic energy spectra obtained from OCO based AN-MPCD collapse when they are multiplied by $\zeta^{1/3}$ and plotted as function of the normalized wave number, k/k^*. This is illustrated in figure S 4 (a) for simulations at $U=15\ k_\mathrm{B}T$. Finally, kinetic energy spectra fall on a single curve when they are plotted as function of the wave number normalized with respect to the velocity correlation length: kl_v, as shown in figure S 4 (b).

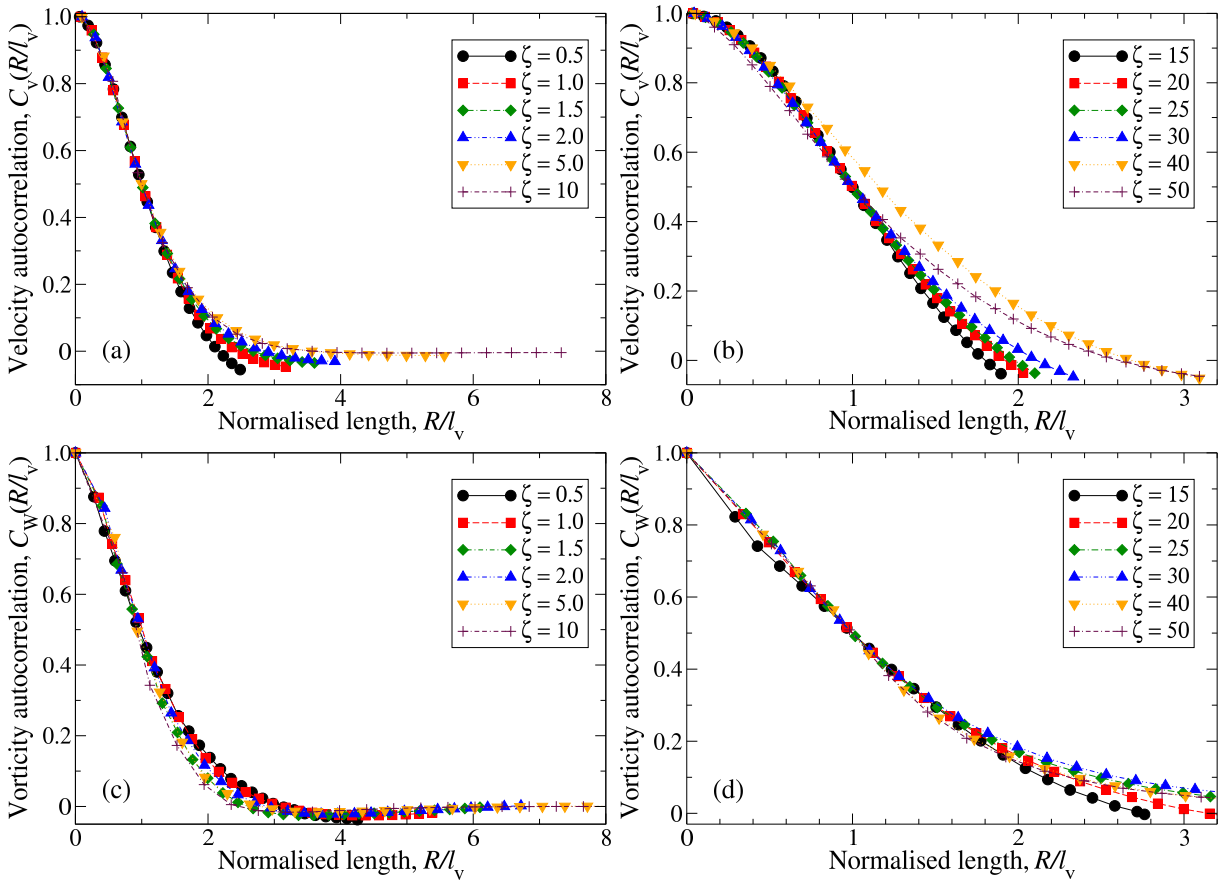

Figure S 2: Flow correlation functions measured with cell-level quantities as function of the normalised distance R/l_v. (a) Velocity autocorrelations in OCO based AN-MPCD at $U = 30k_BT$. (b) Velocity autocorrelations in Hybrid based AN-MPCD. (c) Vorticity autocorrelations in OCO based AN-MPCD at $U = 30k_BT$. (d) Vorticity autocorrelations in Hybrid based AN-MPCD. In all cases ζ is given in units of k_BT/a^3.

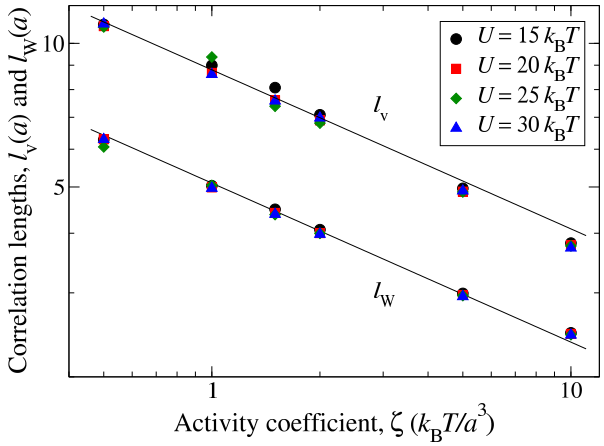

Figure S 3: Velocity and vorticity correlation lengths, l_v and l_W, respectively, in units of the cell size a in OCO based AN-MPCD. Lines indicate the decaying behaviour $\zeta^{-1/3}$.

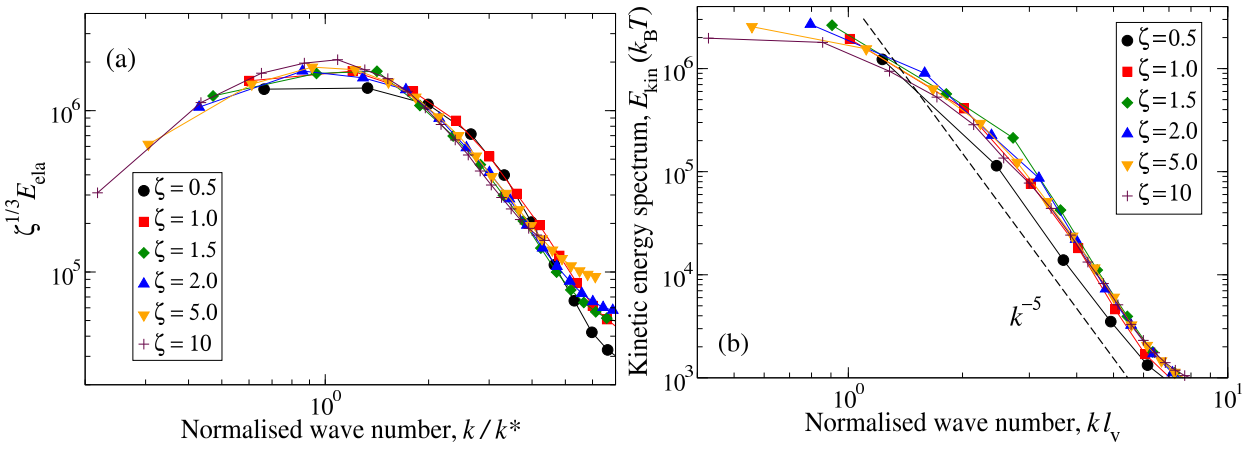

Figure S 4: Collapse of spectra in OCO based AN-MPCD in the case $U = 15k_{\rm B}T$. (a) Elastic energy spectra times $\zeta^{1/3}$ (in units of $(k_{\rm B}T)^{4/3}/a$). The corresponding curves are those in figure 11 (a). Normalisation of k was achieved using k^* values from figure 11 (c). (b) Kinetic energy spectra as function of the dimensionless wave number, $kl_{\rm v}$. The associated data are those in figure 12 (a). $l_{\rm v}$ values were taken from figure 10 (a). In all cases ζ is given in units of $k_{\rm B}T/a^3$.

Movie captions

1. **Movie S1**: Active nematics simulated by OCO based AN-MPCD with activity $\zeta = 0.3k_{\rm B}T/a^3$ show distortions but no creation of disclinations. The following features are valid here and in Movies S2 to S6: the director field at collision cells is illustrated by small bars scaled 4 times, system starts from a state of uniform orientation, movie length corresponds to 2.5×10^4 MPCD steps, and frames are separated by 2×10^2 steps. Large distortions are emphasised by including isosurfaces of order parameter value $S^{\rm c} = 0.75$.

2. **Movie S2**: Nematic liquid crystals simulated by OCO based AN-MPCD with activity $\zeta = 0.4k_{\rm B}T/a^3$ present active turbulence and dynamic disclinations here revealed by isosurfaces of order parameter value $S^{\rm c} = 0.65$.

3. **Movie S3**: Nematic liquid crystals simulated by OCO based AN-MPCD with activity $\zeta = 1.0k_{\rm B}T/a^3$ present active turbulence and dynamic disclinations here revealed by isosurfaces of order parameter value $S^{\rm c} = 0.60$. The density of topological defects increases with ζ as can be observed by comparing this movie with Movie S2.

4. **Movie S4**: Active nematic liquid crystals simulated by Hybrid based AN-MPCD at activity $\zeta = 10k_{\rm B}T/a^3$ thermalizes at a distorted state without disclinations. Large distortions are emphasised by including isosurfaces of order parameter value $S^{\rm c} = 0.65$.

5. **Movie S5**: Hybrid based AN-MPCD simulations at activity $\zeta = 15k_{\rm B}T/a^3$ yield nematics with active turbulence and dynamic disclinations revealed by isosurfaces of order parameter value $S^{\rm c} = 0.50$.

6. **Movie S6**: Hybrid based AN-MPCD simulations at activity $\zeta = 30k_{\rm B}T/a^3$ yield nematics with active turbulence and dynamic disclinations revealed by isosurfaces of order parameter value $S^{\rm c} = 0.45$. The density of topological defects increases with ζ as can be observed by comparing this movie with Movie S5.

7. **Movie S7**: Annihilation of a disclination loop in OCO based AN-MPCD simulations with parameters $U = 25 k_B T$ and $\zeta = 2.0 k_B T/a^3$. These parameters also apply for Movies S8 to S10. Here and in Movies S8 to S14, structures that follow annihilation or creation dynamics are highlighted in orange color while the network of curvilinear disclinations is shown in purple. Also, small cubes with volume of one MPCD collision cell are included to discern the size of the analysed structures.

8. **Movie S8**: A disclination loop merges with the network of topological defects in OCO based AN-MPCD.

9. **Movie S9**: A disclination loop is nucleated from a region without defects in OCO based AN-MPCD.

10. **Movie S10**: The network of curvilinear disclinations in OCO based AN-MPCD emits a defect loop into the bulk.

11. **Movie S11**: Self-annihilation of a disclination loop in Hybrid based AN-MPCD. Here and in Movies S12 to S14, simulations were performed with activity $\zeta = 30 k_B T/a^3$.

12. **Movie S12**: A disclination loop in the bulk merges with the network of topological defects in Hybrid based AN-MPCD simulations.

13. **Movie S13**: Nucleation of a disclination loop in Hybrid based AN-MPCD simulations.

14. **Movie S14**: The network of topological defects in Hybrid based AN-MPCD splits emitting a disclination loop into the bulk.

References

[1] R. J. LeVeque, *Finite Difference Methods for Ordinary and Partial Differential Equations*, Society for Industrial and Applied Mathematics, 2007.

[2] M. P. Allen and D. Frenkel, *Calculation of liquid-crystal frank constants by computer simulation*, *Phys. Rev. A*, 1988, **37**, 1813–1816.

[3] T. N. Shendruk and J. M. Yeomans, *Multi-particle collision dynamics algorithm for nematic fluids*, *Soft Matter*, 2015, **11**, 5101–5110.

[4] H. Híjar, *Dynamics of defects around anisotropic particles in nematic liquid crystals under shear*, *Phys. Rev. E*, 2020, **102**, 062705.

[5] H. Híjar, R. Halver and G. Sutmann, *Spontaneous fluctuations in mesoscopic simulations of nematic liquid crystals*, *Fluct. Noise Lett.*, 2019, **18**, 1950011.

[6] H. Pleiner and H. R. Brand, *Pattern Formation in Liquid Crystals*, Springer, New York, 1996, pp. 15–67.

[7] P. Ilg, I. V. Karlin, and H. C. Öttinger, *Generating moment equations in the Doi model of liquid-crystalline polymers*, *Phys. Rev. E* 1999, **60**, 5783–5787.

[8] M. Kröger and P. Ilg, *Derivation of Frank-Ericksen elastic coefficients for polydomain nematics from mean-field molecular theory for anisotropic particles*, *J. Chem. Phys.*, 2007, **127**, 034903.

[9] M. Kröger, A. Ammar, and F. Chinesta, *Consistent closure schemes for statistical models of anisotropic fluids*, *J. NonNewton. Fluid Mech.*, 2008, **149**, 40–55.

[10] M. Doi and S. F. Edwards, *The Theory of Polymer Dynamics*, Clarendon Press, 1986.

[11] H. Híjar, D. M. de Hoyos, and I. Santamaría-Holek, *Pattern formation from consistent dynamical closures of uniaxial nematic liquid crystals*, *J. Chem. Phys.*, 2012, **136**, 114109.

[12] J. K. G. Dhont, *An Introduction to Dynamics of Colloids*, Elsevier, 1996.